nature communications

Article

https://doi.org/10.1038/s41467-025-66129-5

Sources of essential lipids for *Mycoplasma pneumoniae* via P116 to target liver and atherosclerotic lesions

Received: 18 December 2024

Accepted: 30 October 2025

Published online: 16 December 2025

Check for updates

David Vizarraga[1,2,13], Marina Marcos[3,13], Noemi Rotllan[4,5,13], Jesús Martín[1], David Santos[4,5], Mercedes Camacho[4,6], Begoña Soto[4,7], Lorena Velasco-Reniu[3,4], Pablo Guerra[8], Félix Pareja[9], María Collantes[10,11], Wanlu Wu[3], Irene Rodríguez-Arce[2], Luis Serrano[2,12], Jaume Piñol[3,14] ✉, Ignacio Fita[1,14] ✉ & Joan Carles Escolà-Gil[4,5,14] ✉

*Mycoplasma pneumoniae (MPN) i*s a bacterial pathogen that primarily causes atypical pneumonia. It cannot synthesize certain essential lipids and therefore relies on the host for their acquisition to survive. *MPN* has been detected in increased amounts within ruptured atherosclerotic plaques. In this work, we show that the protein P116 facilitates cholesterol acquisition from LDL, HDL and various cell types. Targeting P116's C-terminal domain with a monoclonal antibody inhibits cholesterol acquisition and bacterial growth in vitro. Phase contrast epifluorescence microscopy of human arteries reveals that this antibody blocks *MPN* binding to atherosclerotic lesions ex vivo. Additionally, an *MPN* chassis injected into hyperlipidemic female mice localizes to the liver and atherosclerotic plaques. Here, we report that P116 plays a role in extracting essential lipids from lipoproteins and host cells and regulates *MPN* localization to atheromatous plaques. The study highlights *MPN*'s potential as a tool for targeting atherosclerotic lesions and fatty liver.

Mycoplasma pneumoniae (MPN) is a facultative intracellular human pathogen that lacks a cell wall and causes community-acquired pneumonia, sometimes leading to severe systemic effects[1]. *MPN* accounts for 40% of community-acquired pneumonia cases[2]. *MPN*, in addition to being a respiratory pathogen, can clinically manifest at extrapulmonary sites in up to 25% of infections[3]. Unlike other significant respiratory pathogens, such as *Streptococcus pneumoniae* and *Haemophilus influenzae*, no vaccine currently exists to address both the pulmonary and extrapulmonary complications associated with *MPN*[4]. Prospective surveillance data indicate a re-emergence of *MPN* in Europe and Asia, with increasing cases reported across various regions[5,6]. With one of the smallest genomes of 816 kbp[7], *MPN* cannot

[1]Instituto de Biología Molecular de Barcelona (IBMB-CSIC), Parc Científic de Barcelona, Barcelona, Spain. [2]Centre for Genomic Regulation (CRG), The Barcelona Institute of Science and Technology, Barcelona, Spain. [3]Institut de Biotecnologia i Biomedicina and Departament de Bioquímica i Biologia Molecular, Universitat Autònoma de Barcelona, Cerdanyola del Vallès, Spain. [4]Institut de Recerca Sant Pau (IR SANT PAU), Barcelona, Spain. [5]CIBER de Diabetes y Enfermedades Metabólicas Asociadas (CIBERDEM), Madrid, Spain. [6]CIBER de Enfermedades Cardiovascular (CIBERCV), Madrid, Spain. [7]Servei d'Angiologia i Cirurgia Vascular i Endovascular, Hospital de la Santa Creu i Sant Pau, Barcelona, Spain. [8]IBMB-CSIC Cryo-Electron Microscopy M Platform. Instituto de Biología Molecular de Barcelona (IBMB-CSIC). Joint Electron Microscopy Center at ALBA (JEMCA), Barcelona, Spain. [9]Unidad de Radiofarmacia, Servicio Medicina Nuclear, Clínica Universidad de Navarra, Pamplona, Spain. [10]Unidad de Imagen Molecular Traslacional (UnIMTRA), Servicio Medicina Nuclear, Clínica Universidad de Navarra, Pamplona, Spain. [11]Instituto de Investigación Sanitaria de Navarra (IdiSNA), Pamplona, Spain. [12]ICREA (Institució Catalana d'Investigació i Estudis Avançats), Barcelona, Spain. [13]These authors contributed equally: David Vizarraga, Marina Marcos, Noemi Rotllan. [14]These authors jointly supervised this work: Jaume Piñol, Ignacio Fita, Joan Carles Escolà-Gil. ✉e-mail: Jaume.Pinyol@uab.cat; ifrcri@ibmb.csic.es; jescola@santpau.cat

synthesize several lipids crucial for its cell membrane structure, including sphingomyelin, phosphatidylcholine, and cholesterol[8,9]. Unesterified cholesterol, a rare component among prokaryotes, is vital for *MPN* cells and constitutes one of the most abundant lipids in their membranes[10]. Our recent research has revealed the structure of the immunogenic and essential protein P116 from *MPN*[11]. The 116 kDa P116 subunits feature two extracellular domains—a small N-terminal domain and a large C-terminal or core domain—that are anchored to the mycoplasma membrane via a flexible linker[11]. The C-terminal domain exhibits a unique fold resembling a half-open hand, characterized by a large β-sheet, the palm, and by pairs of antiparallel amphipathic α-helices, the fingers, that collectively form a vast hydrophobic, lipid-binding cavity. The fingers flexibility allows the cavity volume to vary according to the lipid cargo. The cavity appears to exhibit significant specificity for lipids crucial for the growth of *MPN*[11].

MPN and *Chlamydia pneumoniae* have been detected in increased quantities within ruptured atherosclerotic plaques[12,13]. These pathogens have been associated with adventitial inflammation and positive vessel remodeling in thrombosed coronary arteries of patients who suffered acute myocardial infarction[14]. Additionally, experimental studies have demonstrated that inoculation with both agents exacerbates atherosclerosis in the aortas of hyperlipidemic mice[15].

Low-density lipoproteins (LDLs) and high-density lipoproteins (HDLs) are characterized by their content of apolipoprotein (apo)B-100 and apoA-I, respectively, and their major lipid components are cholesterol esters and phospholipids, with a smaller amount of unesterified cholesterol. The function of LDL is primarily the transport and delivery of cholesterol to cells, including peripheral tissues and the liver, while HDL transports cholesterol to steroidogenic tissues[16]. Accumulation of oxidatively modified LDL in the subendothelial space induces its uptake by macrophages, promoting foam cell formation and a wide range of bioactivities that drive the development of atherosclerotic lesions. In contrast, HDL promotes macrophage cholesterol efflux to reduce lesion formation[17]. Since, as mentioned above, *MPN* cannot synthesize several lipids essential for its cell membrane structure, it must obtain these lipids from the blood or arterial lining cells to survive in the bloodstream and localize at atherosclerotic plaques.

In this work, we assessed the capacity of P116 to extract the *MPN* essential lipids from circulating human lipoproteins and from cells. We also investigated the role of P116 in mediating the localization of *MPN* to human atherosclerotic lesions ex vivo. Moreover, using a genetically engineered *MPN* chassis, we determined the bacterium's ability in vivo to reach the liver and atheroma plaques via the bloodstream in hyperlipidemic mice, unveiling a biotechnological approach for studying and treating atherosclerotic and hepatic lesions.

Results

Human LDL is a source of unesterified cholesterol for MPN P116

Since both LDL and HDL are major cholesterol-carrying lipoproteins in human plasma and are responsible for supplying cholesterol to tissues, we initially measured the rate of radiolabeled unesterified cholesterol transfer from LDL or HDL to *MPN* and the protein P116 (see the schematic diagram of the experimental design in Fig. 1a). The rate of cholesterol transfer from these lipoproteins to *MPN* and P116 was measured at equal concentrations of their main apolipoproteins (see supplementary Fig. 1 for lipoprotein composition). In all experiments, the main LDL protein (ApoB100) and HDL protein (apoA1) were not detected, cross-checked by immunoturbidimetric detection, verifying that no LDL and HDL had contaminated the purified *MPN* and P116 samples. When LDL containing radiolabeled unesterified cholesterol was incubated with MPN, a significant portion of the LDL-derived radiotracer was transferred to the subsequently isolated MPN, whereas transfer was less efficient when incubating with HDL (Fig. 1b). Similar patterns were observed when LDL or HDL were incubated directly with P116 (Fig. 1c). A time-dependent experiment was performed in which LDL containing radiolabeled cholesterol was incubated with unlabeled P116 for up to 90 min. Under these conditions, the quantity of labeled cholesterol in isolated P116 increased rapidly during the incubation, reaching a maximum plateau after 45 min (Fig. 1c, inset).

Human lipoproteins transfer multiple lipids to P116

We conducted a detailed ultra-high-performance liquid chromatography-mass spectrometry (UHPLC-MS) analysis of the lipid species in the isolated P116 fraction after incubation with human LDL or HDL under the same experimental conditions described for the isotopic method (Fig. 1d). We identified 370 lipid species in the isolated P116 fractions. In empty P116, most of these lipid species were not detected, except for some triacylglycerol species with low relative intensity (Supplementary Data). In P116 samples refilled with LDL or HDL, we observed a striking accumulation of phosphatidylcholines, triacylglycerols, and sphingomyelins, with triacylglycerols being relatively more abundant in HDL-refilled P116, whereas sphingomyelins were lower (Fig. 1e). Unesterified sterols (cholesterol and derivatives) were higher in P116 after incubation with LDL, in contrast to esterified cholesterol, which was detected in significant amounts after incubation with both LDL and HDL, and was particularly enriched in HDL-refilled P116 (Fig. 1e).

P116 acquires cholesterol from diverse cell types

We then adapted a method used for evaluating unesterified cholesterol efflux stimulated by HDL and lipid-free apoA1 from macrophages to evaluate the potential of P116 to extracts unesterified cholesterol from the human pulmonary cell membrane (see the schematic diagram of the experimental design in Fig. 2a). When pulmonary cells containing radiolabeled unesterified cholesterol were incubated with P116 in the media, a significant fraction of radiotracer was detected in the isolated P116, although the transfer was significantly lower to that to the main physiological acceptor, HDL (Fig. 2a). We also evaluated the potential of P116 to acquire unesterified cholesterol from cholesterol-loaded Chinese hamster ovary (CHO) cells, CHO cells overexpressing scavenger receptor type B1 (SR-BI), and macrophages before and after activation of the cholesterol efflux transporters ATP-binding cassette (ABC)A1 and ABCG1 (Fig. 2b, c). As observed with pulmonary cells, a portion of the radiotracer was recovered in isolated P116 following incubation with cholesterol-loaded CHO cells and macrophages (Fig. 2b, c). In contrast to HDL, P116-mediated cholesterol uptake was unaffected by SR-BI expression (Fig. 2b). Furthermore, while activation of ABCA1 and ABCG1 promotes cholesterol efflux to classical acceptors such as HDL or lipid-free apoA-I, upregulation of these transporters did not enhance cholesterol transfer to P116 (Fig. 2c). Notably, the ability of P116 to acquire unesterified cholesterol from cell membranes was highly correlated with the cellular cholesterol content (Supplementary Fig. 2). These findings suggest that P116 bypasses canonical receptor-mediated uptake or efflux mechanisms and instead captures freely available or loosely bound unesterified cholesterol. Furthermore, inhibition of lipase activity with orlistat also had no effect on P116-mediated uptake (Supplementary Fig. 3).

The analysis of the lipid species in the isolated P116 fraction after incubation with human pulmonary cells also identified 276 lipid species, but their relative intensity in P116 was very low in comparison with that of the isolated P116 incubated with lipoproteins (Fig. 2d and supplementary Data).

Effects of antibodies targeting the C-terminal domain of P116

To dissect the immunogenic activity of P116, we produced three different constructs: P116/30-957 (residues 30 to 957), a derivative lacking the C-term region (P116/30-845), and a derivative lacking also the N-terminal domain (P116/246-818)[11]. The three constructs were tested with total sera from twenty-five patients with positive diagnostic for

https://doi.org/10.1038/s41467-025-66129-5

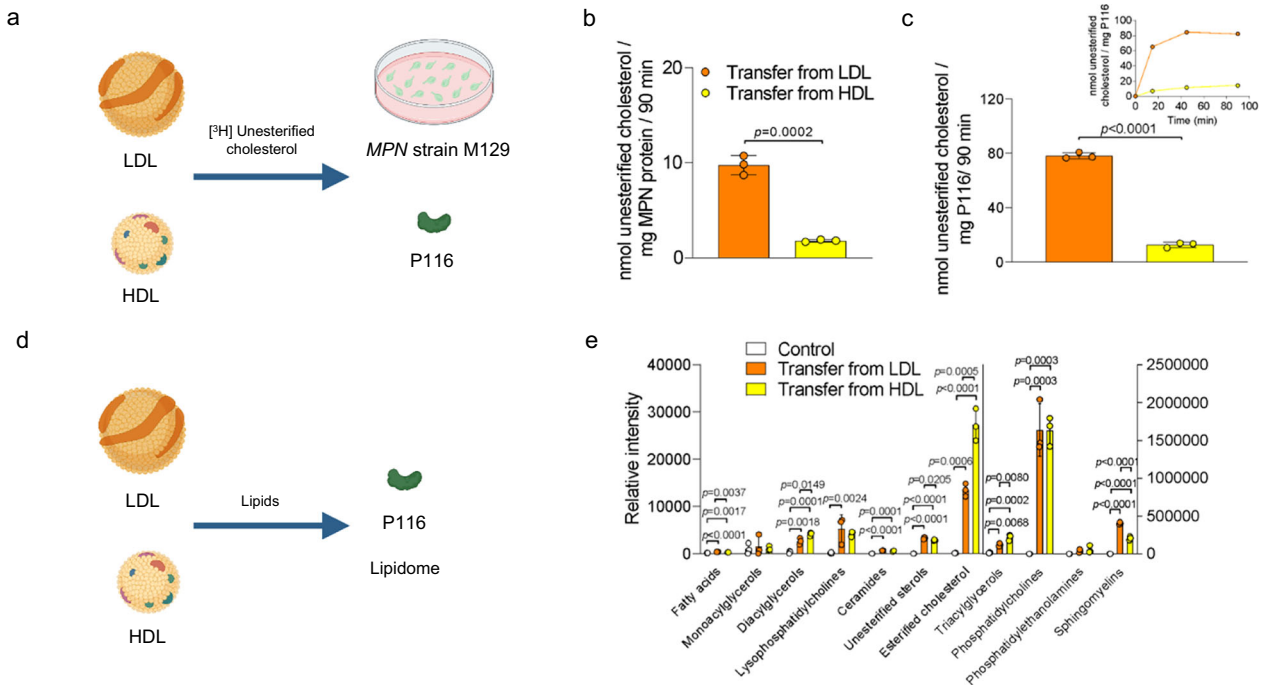

Fig. 1 | Human low-density lipoproteins (LDLs) and high-density lipoproteins (HDLs) as sources of essential lipids for P116. a Schematic representation of isotopic unesterified cholesterol transfer and lipidomic analyses. LDL or HDL (0.5 mg/mL) were radiolabeled with [1,2-^{3}H(N)] unesterified cholesterol and incubated with cultured *Mycoplasma pneumoniae (MPN)* strain M129 or P116 (0.25 mg/mL) at 37 °C. Adherent *MPN* were isolated from culture flasks, and P116 was purified using a HisTrap HP affinity column. Radiolabeled cholesterol in *MPN* and P116 was quantified by liquid scintillation counting. **b**, **c** Relative transfer of radiolabeled unesterified cholesterol from LDL and HDL to *MPN* and P116 for 90 min at 37 °C. **c inset** Time-course analyses of the transfer of radiolabeled unesterified cholesterol from LDL and HDL to P116 at 37 °C. **d** In separate experiments, non-radiolabeled HDL or LDL were incubated with P116, and lipid species were analyzed by ultra-high-performance liquid chromatography–mass spectrometry (UHPLC–MS). P116 protein that was isolated and incubated under identical conditions, but without LDL, HDL was used as control. **e** Main lipid classes identified by UHPLC–MS analyses, showing lipid class distribution in P116 before and after incubation with LDL or HDL. Data show the sum of normalized areas for all metabolites with the same chemical characteristics. Two y-axes are shown with different scales: the left axis corresponds to fatty acids, monoacylglycerols, diacylglycerols, lysophosphatidylcholines, ceramides, unesterified sterols, and esterified cholesterol; the right axis (larger scale) corresponds to phosphatidylcholines, triacylglycerols, sphingomyelins, and phosphatidylethanolamines. Values are mean ± SD of three independent experiments. **b**, **c** A two-sided unpaired t-test was used for LDL vs. HDL radiolabeled unesterified cholesterol transfer to P116. **e** One-way ANOVA with Tukey's multiple comparisons tested differences in lipid species amounts between groups. Schematic illustrations were created in BioRender. Rotllan, N. (2025) https://BioRender.com/8j7tzf5.

MPN based on serological tests and six uninfected subjects. Sera from uninfected individuals exhibited very low reactivity against any of the P116 constructs compared with infected patients (Supplementary Fig. 4). All infected patients were positive for the P116/30-957 construct (Supplementary Table 1). We obtained identical results when we used the P116/30-845 construct. However, the P116/246-818 construct resulted in a significant decrease in positive sera (72%) compared to the P116/30-957 and P116/30-845 constructs (Supplementary Table 1). Importantly, the overall signal of the P116/30-957 and P116/30-845 constructs was higher than that obtained with P116/246-818 (Fig. 3a).

A panel of antibodies against P116 (residues 30–957) was tested, and all except one targeted the core domain of P116 and showed inhibitory effects on *MPN* growth and adhesion. Based on these results, monoclonal antibody (mAb) 3G9 was selected for further experiments as it produced the strongest inhibitory effect. We also used mAb 3B5, which lacks specificity for the central region of P116 and exhibits lower affinity. The structure of the P116-mAb–3G9 complex determined by Cryo-EM (Supplementary Fig. 5), showed that the epitope is located in four α-helices forming two of the fingers that define the hydrophobic cavity of P116 (Fig. 3b and Supplementary Fig. 6)[11], and indicates that mAb-3G9 hinders the fingers flexibility required by the functioning of P116. Importantly, pre-incubation of P116 with mAb-3G9, followed by incubation with radiolabeled LDL, resulted in a notable reduction in the amount of radiolabeled cholesterol recovered in the post-incubated, isolated P116 fraction (Fig. 3c). This effect was not observed when P116 was incubated with mAb-3B5. Furthermore, mAb-3G9 not only blocked cholesterol transfer but also significantly inhibited the growth of cultured mycoplasma cells compared with mAb-3B5 (Fig. 3d). These results suggest that targeting the C-terminal domain of P116 in *MPN* infections could represent a potential therapeutic strategy.

Antibody effects on MPN localization to atherosclerotic plaques

We assessed the ability of *MPN* to adhere to human carotid atherosclerotic plaques using cell culture invasion assays. For this purpose, we used the *MPN* strain M129 expressing the fluorescent protein Venus[18]. Cells were cultured in the presence of human atherosclerotic carotid tissue fragments, with distal healthy tissue as a control (see the schematic diagram of the experimental design in Fig. 4a). After inoculation, growth was monitored at 0–48 h by phase contrast and epifluorescence microscopy. Although the tissue exhibited some autofluorescence, the presence of mycoplasma cells could be detected. Compared to the control healthy tissue, mycoplasma cell localization and growth were significantly higher in the vicinity of the atherosclerotic tissue (Fig. 4b).

In line with the cell growth inhibition by mAb–3G9, this antibody, which interacts with the C-terminal domain of P116, also interfered with the presence of *MPN* cells in the atherosclerotic tissue (Fig. 4b and Supplementary Fig. 7). This effect was not observed when *MPN* cells were incubated with P116 mAb-3B5, which exhibits no specificity to the

https://doi.org/10.1038/s41467-025-66129-5

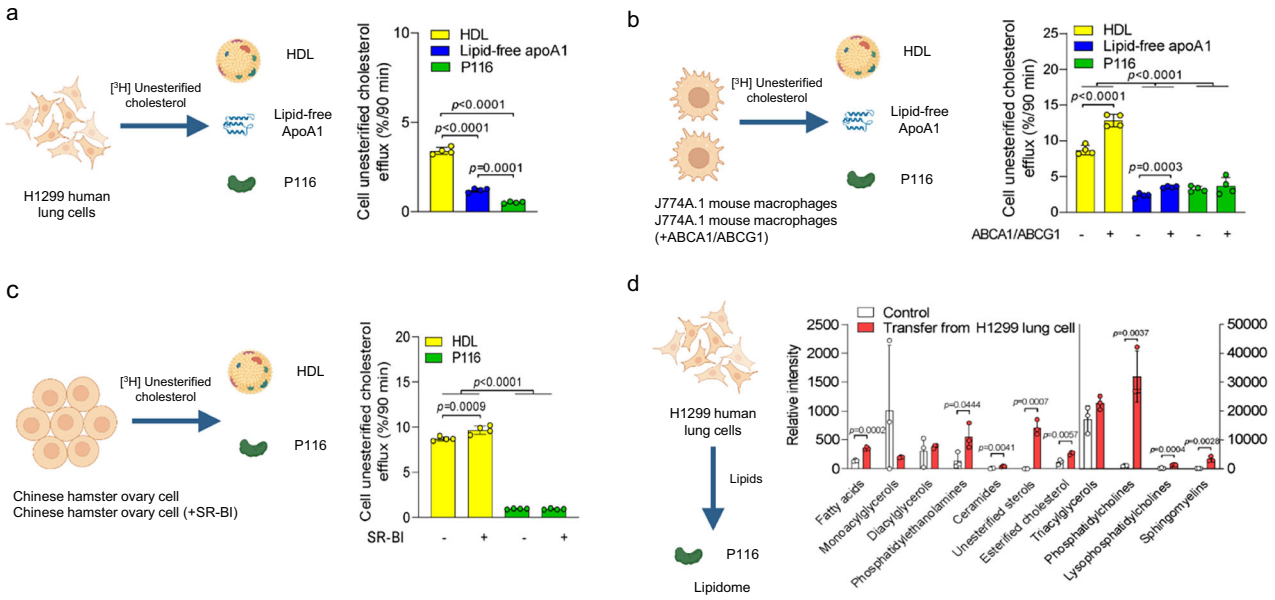

Fig. 2 | P116 acquires cholesterol from diverse cell types. a H1299 lung cells (3×10^5) radiolabeled with [1,2-^{3}H(N)] unesterified cholesterol was incubated for 90 min at 37 °C with high-density lipoproteins (HDL, 0.1 mg/mL), lipid-free apolipoprotein (apo)A1 (0.1 mg/mL), or P116 (0.1 mg/mL). P116 was isolated from the medium, and radiolabeled cholesterol quantified by liquid scintillation counting; adherent radiolabeled cells were also analyzed. **b** J774.A1 mouse macrophages (3×10^5) were radiolabeled with [1,2-^{3}H(N)] unesterified cholesterol and equilibrated in the presence or absence of the liver X receptor agonist T0901317 (2 µM) to activate ATP-binding cassette (ABC)A1/ABCG1 pathways. Cells were then incubated with HDL, lipid-free apoA1, or P116, and cholesterol efflux was quantified under baseline conditions or after transporter activation. **c** Schematic of cholesterol transfer from Chinese hamster ovary (CHO) cells and CHO cells expressing SR-BI (3×10^5), radiolabeled and incubated with HDL or P116 as in (**a**). Data in (**a**–**c**) show in vitro cholesterol efflux from each cell type. Values are mean ± SD of four independent experiments. One-way ANOVA with Tukey's multiple comparisons tested differences between groups. Efflux from J774.A1 mouse macrophages to apoA-I before and after ABCA1/G1 activation was compared using a two-sided unpaired t-test. **d** H1299 lung cells were incubated with P116 (0.25 mg/mL), and lipid species were analyzed by UHPLC–MS. Main lipid classes are shown for P116 and for P116 after incubation with H1299 cells. Data represent the sum of normalized metabolite areas with shared chemical characteristics ($n = 3$ independent samples per group). Two y-axes are shown with different scales: the left axis corresponds to fatty acids, monoacylglycerols, diacylglycerols, lysophosphatidylcholines, ceramides, unesterified sterols, and esterified cholesterol; the right axis (larger scale) corresponds to phosphatidylcholines, triacylglycerols, sphingomyelins, and phosphatidylethanolamines. Values are mean ± SD. Statistical significance was assessed using a two-sided unpaired t-test. Schematic illustrations were created in BioRender. Rotllan, N. (2025) https://BioRender.com/ehvrs5v.

central region of P116 (residues 246–818). Importantly, we quantified the percentage increase in *MPN*-positive area from 0 to 48 h across four independent carotid artery specimens (Fig. 4c). Incubation with mAb-3G9 caused a significant reduction in *MPN* growth compared with atherosclerotic plaques incubated without antibody or with mAb-3B5, with values comparable to those observed in healthy tissue.

Biotransfer of MPN in hyperlipidemic mice

We further investigated whether *MPN* could colonize various organs in vivo using single-photon emission computed tomography (SPECT/CT) imaging. This was achieved by intravenously injecting a radiolabeled non-pathogenic *MPN* chassis into C57BL/6 wild-type mice and a hyperlipidemic mouse model (see the schematic diagram of the experimental design in Fig. 5a). We specifically used female LDL receptor knockout mice ($LDLR^{-/-}$) on a C57BL/6 background, which develop hyperlipidemia and atherosclerosis when fed a Western-type diet, a high-fat, cholesterol-rich regimen (Supplementary Fig. 8). The biodistribution of radiolabeled *MPN* chassis revealed strong signal intensity in the livers of both female wild-type and $LDLR^{-/-}$ mice (Fig. 5b). As expected, wild-type mice accumulated substantial amounts of cholesterol in the liver after being fed a Western diet, but this accumulation was significantly greater in $LDLR^{-/-}$ mice (Fig. 5c). Consistent with the biodistribution data, the total hepatic *MPN* load—measured by both radioactivity and qPCR—was comparable between the two groups (Fig. 5d, e). No significant correlation was observed between liver cholesterol content and radiolabeled *MPN* abundance (Fig. 5f), indicating that liver accumulation does not scale directly with hepatic cholesterol levels.

Using SPECT/CT imaging, we observed that *MPN* chassis localized specifically to areas containing atherosclerotic lesions, but only in $LDLR^{-/-}$ mice, which develop atherosclerosis under high-fat diet conditions (Fig. 5g–i). Finally, no signal from the radiolabeled *MPN* chassis was detected in the lungs. These observations confirm the effective tropism of *MPN* toward livers and atherosclerotic plaques.

Discussion

MPN lacks the capacity to synthesize several essential lipids, including cholesterol, and thus relies on host-derived lipids for survival[19]. P116 is an essential and highly immunogenic protein required for the viability of *MPN* and has been reported to contribute to host cell adherence[20], although this function is mainly mediated by the Nap complex (P1 and P40/P90 proteins)[21]. We recently demonstrated that the P116 structure features a novel fold, including an unusually large hydrophobic cavity filled with lipid ligands[11]. Mass spectrometry and radioactivity transfer experiments revealed the ability of P116 to extract various lipids from fetal bovine serum and cholesterol from HDLs[11].

In this study, we demonstrate that human LDLs can serve as an efficient source of unesterified cholesterol for both P116 and intact *MPN* cells, with markedly higher transfer rates compared to HDLs when assessed in vitro at equivalent major protein concentrations, i.e., at comparable numbers of lipoprotein particles. The amount of unesterified cholesterol per particle and its location on the surface of the lipoprotein[22] could explain this accelerated transfer from LDLs to P116. Furthermore, LDLs also efficiently transfer a large variety of sphingomyelin species. Importantly, phosphatidylcholine species, which are also located on the surface of lipoproteins, were the major lipids found

https://doi.org/10.1038/s41467-025-66129-5

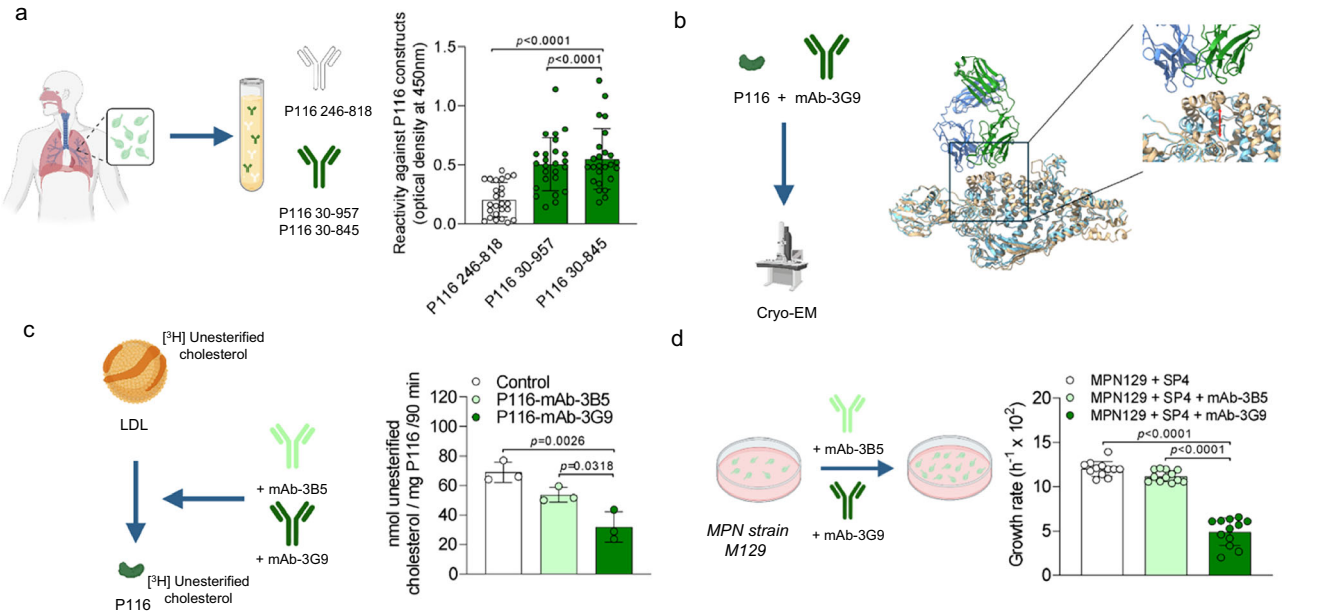

Fig. 3 | C-terminal P116 antibodies impair P116-cholesterol acquisition and *Mycoplasma pneumoniae* (*MPN*) growth. a Reactivity of *MPN*-infected patient sera against P116 constructs; ELISA results are shown for 25 human subjects. **b** Superposition of P116 structures in the full state (tan) with monoclonal antibody (mAb)-3G9 bound (heavy chain, blue; light chain, green) and in the empty state (cyan). The epitope spanning residues 402–430 is highlighted, with the red arrow indicating its positional shift between empty and full conformations. The cryo-EM structure of the P116–mAb 3G9 complex reveals the epitope restricted to four amphipathic α-helices that form two "fingers" shaping the hydrophobic lipid-binding cavity of P116. **c** Relative transfer of radiolabeled unesterified cholesterol from LDL to P116 was measured after incubation with monoclonal antibodies mAb-3B5 or mAb–3G9 under the conditions described in Fig. 1 ($n = 3$ independent replicates per group). **d** mAb-3G9 significantly inhibited the growth of cultured *MPN* strain M129 in SP4 medium compared with both the control and mAb-3B5, which showed no inhibitory effect ($n = 12$ independent replicates per group). Values are mean ± SD. One-way ANOVA with Tukey's multiple comparisons tested group differences. Schematic illustrations were created in BioRender. Rotllan, N. (2025) https://BioRender.com/zha7oke.

in P116 after being incubated with either LDLs or HDLs. The presence of the hydrophobic cavity in P116 and its structure allows the interaction with the amphipathic phospholipids, facilitating the uptake and exchange of these lipid species. In contrast, the elongated architecture of P116 may allow it to align along the HDL surface, facilitating deeper insertion and enhanced access to the hydrophobic core, which could explain its effectiveness in mediating the uptake of triacylglycerol and cholesteryl esters from HDL[23]. Thus, this work demonstrates that human LDLs serve as a key source of unesterified cholesterol, phosphatidylcholines, and sphingomyelins to P116 from *MPN*. HDLs primarily provide phosphatidylcholines, esterified cholesterol, and triacylglycerols to P116. Although these findings remain to be validated in vivo, they suggest that the relative abundance of LDL in circulation could potentially make it a particularly important source of unesterified cholesterol and other essential lipids for *MPN* during infection.

P116 is also capable of inducing the efflux of unesterified cholesterol from lung and ovarian cells and from macrophages although with lower efficiency compared to HDL particles. It should be noted that HDLs are complex lipoproteins with a larger surface area relative to volume and contains apoA-I, which facilitate unesterified cholesterol efflux from cells by interacting with specific transporters on the cell membrane (SR-BI, ABCA1 and ABCG1), as well as through passive diffusion[22]. By contrast, our data show that upregulation of these transporters did not enhance cholesterol transfer to P116, suggesting that P116 does not exploit canonical efflux pathways. Furthermore, inhibition of lipase activity using orlistat did not alter lipid uptake, ruling out a lipase-dependent mechanism. Instead, our findings support a model in which P116 directly extracts freely available or loosely bound lipids from LDL, HDL and host membranes. This is further supported by the observation that cholesterol acquisition was highly correlated with cellular cholesterol content, consistent with a diffusion-driven process.

Our lipidomic analyses revealed that P116 also acquires a broad spectrum of lung cell phosphatidylcholines, albeit less efficiently than from LDL and HDL. Overall, these results demonstrate the versatility of P116 as a microbial lipid acquisition system, enabling mycoplasmas to extract essential lipids from diverse host sources and thereby colonize different tissues.

These findings can be further understood considering the unique lipid requirements of *MPN* membranes, which differ markedly from those of most other bacteria. Unlike typical bacteria, which synthesize their own phospholipids, Mycoplasma species rely almost entirely on the host for exogenous lipids—particularly cholesterol, phosphatidylcholine, and sphingomyelin[24–27]. Cholesterol can constitute 30–50% of the membrane lipids—far higher than in most bacteria—where it contributes to stabilization and rigidity[25]. Phosphatidylcholine helps maintain membrane fluidity, while sphingomyelin supports lipid raft formation, potentially facilitating host–pathogen interactions[25,26,28]. Recent high-resolution lipidomics has further highlighted the remarkable plasticity of these membranes, showing that lipid composition can shift dynamically in response to environmental stressors such as temperature changes[29]. These characteristics align closely with our lipidomic findings, which show that P116 can acquire not only cholesterol but also phosphatidylcholine and sphingomyelin. Taken together, these observations reinforce the concept that P116 functions as a broad lipid scavenger, supplying *MPN* with essential components to sustain its unusual and highly adaptable membrane composition[8]. This inherent plasticity may also help explain how P116-mediated lipid acquisition supports bacterial survival across diverse host environments and contributes to its capacity for colonization beyond the respiratory tract. Our data do not support a role for P116 as a classical adhesin. Unlike the Nap complex, P116 does not exhibit high-affinity or saturable binding to host cells. Rather, its structural features and functional behavior are consistent with a role in lipid scavenging,

https://doi.org/10.1038/s41467-025-66129-5

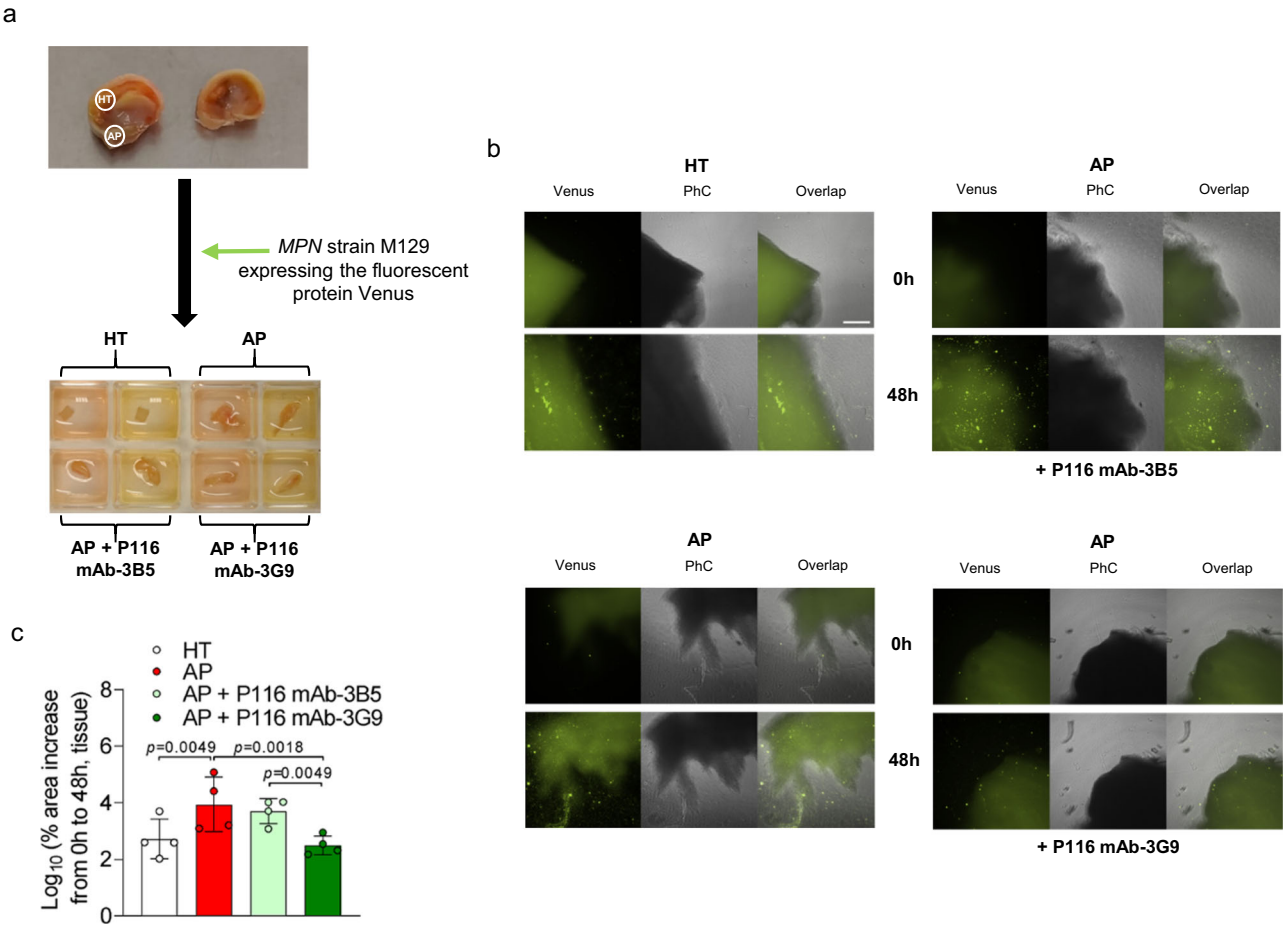

Fig. 4 | C-terminal P116 antibodies reduce *Mycoplasma pneumoniae (MPN)* localization to human atherosclerotic plaques ex vivo. a Experimental workflow for evaluating *MPN* strain M129 localization. *MPN* cells expressing the fluorescent protein Venus were incubated with fragments of healthy human non-atherosclerotic tissue (HT) or human atherosclerotic plaque tissue (AP) obtained from carotid sections. Localization was assessed using phase contrast (PhC) and epifluorescence microscopy at 0 h and 48 h post-incubation. **b** Representative Venus fluorescence, PhC, and merged images showing *MPN* localization in HT and AP tissues in the absence or presence of monoclonal antibody (mAb)-3G9 or mAb-3B5. Scale bar = 200 μm. Time-lapse sequences are shown in Supplementary Fig. 7. **c** Quantification of the percentage increase in fluorescent area from 0 h to 48 h in four independent biological replicates. Incubation with mAb-3G9 significantly reduced *MPN* expansion in AP tissue compared with AP alone or AP incubated with mAb-3B5, with values similar to those observed in HT. Values are mean ± SD. One-way ANOVA with Holm-Sidak's multiple comparisons tested differences between groups.

where the hydrophobic cavity directly acquires host lipids without receptor engagement.

Our study suggests that P116 may serve as an immunological target. Antibodies targeting the N-terminal domain of P116, such as mAb-3B5, appear less effective at inhibiting its function. By contrast, mAb-3G9, which recognizes an epitope in the C-terminal domain, interfered with P116-mediated uptake of unesterified cholesterol and directly inhibited mycoplasma growth. This effect is consistent with mAb-3G9 binding to the C-terminal domain of P116, which appears to modulate the size of its hydrophobic cavity to accommodate lipid cargo. Serological analyses revealed that *MPN*-infected patients generate antibodies against both the N- and C-terminal domains of P116 in roughly equal proportions. As antibodies targeting the N-terminal region do not block function, this distribution may reduce the overall protective capacity of the immune response. These findings support consideration of the C-terminal domain of P116 as a possible candidate for vaccine development.

Previous studies have found a higher prevalence of *MPN* in patients with cardiovascular diseases compared to healthy controls[30,31], although a direct causal link has not been demonstrated in humans. Given that ruptured atherosclerotic plaques have shown increased quantities of *MPN*[12,13], we further investigated the potential localization of *MPN* in atherosclerotic lesions ex vivo. Compared to healthy control tissue, mycoplasma cell localization was notably increased around lipid-rich atherosclerotic tissue. Consistent with its observed inhibition of cell growth and cholesterol uptake, mAb−3G9 impaired the binding and proliferation of *MPN* cells in atherosclerotic tissue, highlighting its potential for treating both pulmonary and extrapulmonary *MPN* infections. By limiting *MPN* colonization in vulnerable areas, this mAb against P116 could help reduce the risk of infections or complications associated with atherosclerosis.

In vivo biodistribution studies showed that *MPN* accumulates primarily in the liver and, in LDLR$^{-/-}$ mice with established atherosclerosis, within aortic plaques. Liver accumulation was also observed in wild-type mice, consistent with the liver's central role in lipid processing[32]. Although *MPN* abundance in the liver did not correlate directly with cholesterol content, the elevated hepatic lipid levels in both mouse models may create a permissive environment that facilitates *MPN* tropism, independently of LDLR status, particularly at the 6-hour post-injection time point before any bacterial replication occurs. In contrast, plaque-specific accumulation was observed only in LDLR$^{-/-}$ mice, highlighting the requirement for lesion-associated features such as lipid deposition and altered endothelium.

https://doi.org/10.1038/s41467-025-66129-5

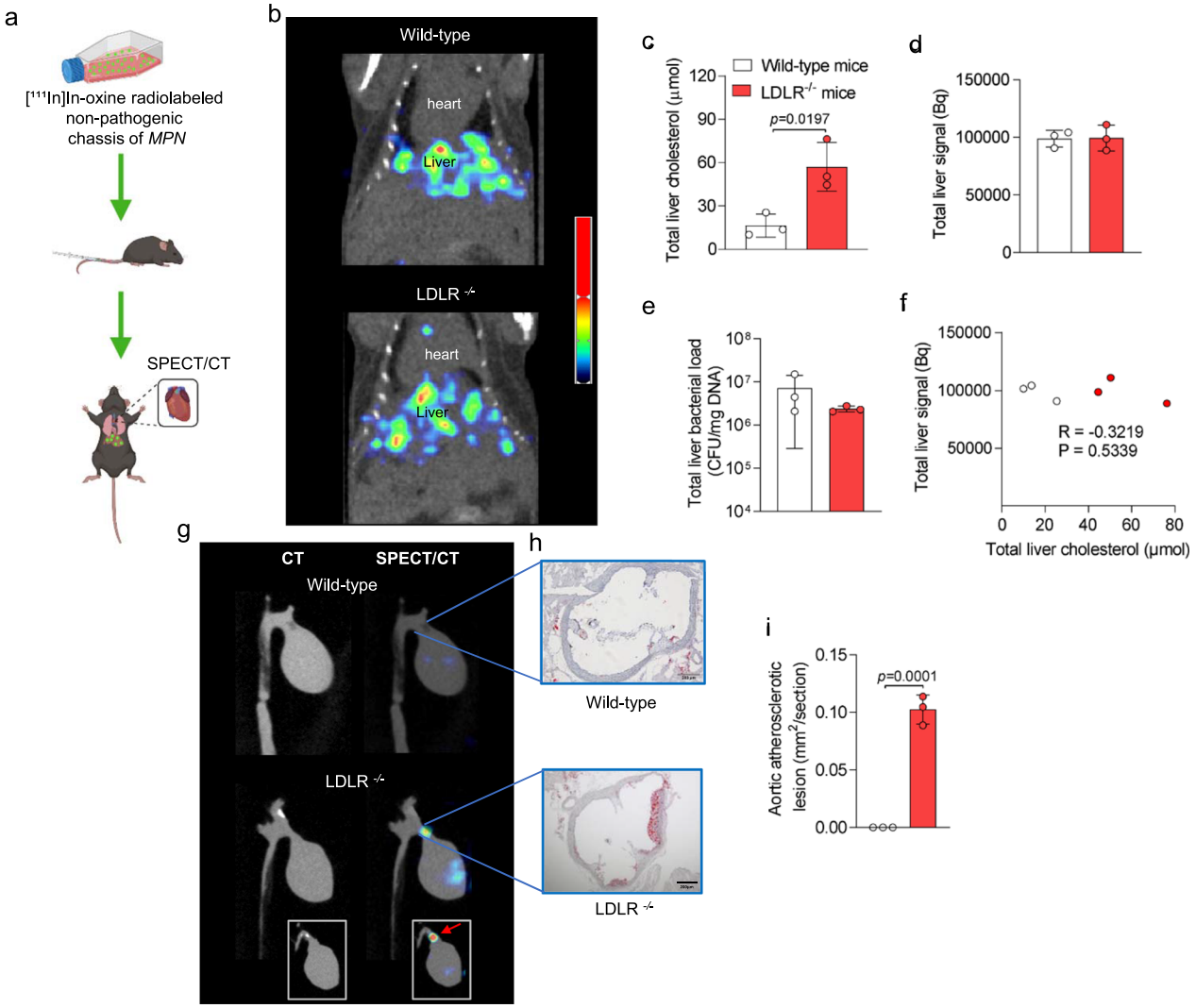

Fig. 5 | Biodistribution of [^{111}In]In-oxine radiolabeled *Mycoplasma pneumoniae (MPN)* chassis. a Radiolabeled *MPN* cells were injected intravenously, followed by whole-body imaging 6 h post-administration and ex vivo heart analysis. **b** In vivo biodistribution of the non-pathogenic MPN strain CV8 evaluated using single photon emission computed tomography (SPECT/CT). **c** Hepatic cholesterol levels in female wild-type and low-density lipoprotein (LDL) receptor knockout (LDLR$^{-/-}$) mice after 8 weeks on a Western-type diet. **d** Total liver radiolabeled signal (Bq) in wild-type and LDLR$^{-/-}$ mice. **e** Liver bacterial load measured by qPCR. **f** Association between liver signal and hepatic cholesterol levels (Pearson's correlation). **g** Representative ex vivo SPECT/CT coronal slices of the heart and aorta of wild-type and LDLR$^{-/-}$ mice at 6 h post-administration. Left, CT images; right, SPECT overlays with radiolabeled signal (red arrow). **h** Representative proximal aortic sections from wild-type and LDLR$^{-/-}$ mice stained with Oil Red O and counterstained with hematoxylin. **i** Quantification of atherosclerotic lesion area in the aortic root of the same groups after diet. Values are mean ± SD, *1q2w453eqwsaxz* = 3 per group. A two-sided unpaired t-test was used for group comparisons. Schematic illustrations were created in BioRender. Rotllan, N. (2025) https://BioRender.com/srns7ds.

Importantly, *MPN* infection has been associated with liver disease, particularly in children[33] underscoring the broader clinical relevance of its tropism for this lipid-rich tissue. Thus, the availability of nutrients directing *MPN* cells toward specific tissues may partly explain the organism's tissue colonization and its association with various non-respiratory symptoms and conditions[34]. While antibody-mediated inhibition effectively blocked *MPN* binding ex vivo, translating this efficacy into in vivo systems is likely to be more complex. Physiological factors such as systemic lipid availability, tissue-specific vascular architecture, and passive lipid access may override or circumvent antibody-mediated inhibition. Further investigation will therefore be required to evaluate the potential of mAb-3G9 and related antibodies under in vivo conditions. Overall, these findings suggest that *MPN* localization to lipid-rich tissues and its interaction with inflammatory microenvironments could influence disease progression. Nonetheless, our results primarily characterize the biodistribution of the engineered chassis as a foundation for exploring its therapeutic potential.

Our findings underscore the concept that P116 plays a role in extracting essential lipids from lipoproteins and from a diversity of cell types, which can explain the colonization of different tissues by *MPN*. In addition, a mAb targeting the C-terminal domain of P116, which reduces cholesterol extraction, inhibits mycoplasma growth in culture, and blocks *MPN* binding to human lipid-rich atherosclerotic lesions ex vivo, demonstrates therapeutic potential. The presence of *MPN* in the liver and atheroma plaques in vivo suggests the potential use of the *MPN* chassis, engineered as a genetically modified biological pill[35], as an innovative biotechnological tool for studying and treating liver diseases, such as fatty liver and liver cancer, as well as atherosclerotic lesions.

Methods

This research complies with all relevant ethical regulations. Human plasma samples were obtained in accordance with the Declaration of Helsinki and institutional ethical guidelines. Eligible donors for

lipoprotein collection were normolipidemic and normoglycemic, with no personal or family history of premature coronary artery disease, major cardiovascular risk factors, or known infectious or inflammatory conditions. All participants provided written informed consent before participation. The study protocol was approved by the Ethical Committee of Hospital de la Santa Creu i Sant Pau (protocol code IIBS-APO-2013-105). The protocols for studies involving infected and uninfected patients were approved by the Ethical Committees of Parc Taulí (Ref 2019/664) and Vall d'Hebron University Hospitals (PR(AG)24/2020). The study involving carotid endarterectomy specimens was approved by the Ethical Committee of Hospital de la Santa Creu i Sant Pau (protocol code IIBSP-LPM-2019-94).

Animal handling and procedures followed the current European (Directive 86/609/EEC) and National (Real Decreto 53/2013) legislations as well as the FELASA and ARRIVE guidelines and obtained the approval of the Animal Experimentation Ethic Committee of Clinica Universidad de Navarra (Code: 096-23).

Cloning, expression, and purification of P116 constructs

Regions corresponding to the *mpn_213* gene from *MPN* were amplified from synthetic clones using different primers for each construct: $P116F_{30}$ and $P116R_{957}$ for P116(30–957); $P116F_{30}$ and $P116R_{845}$ for P116(30–845); $P116F_{246}$ and $P116R_{818}$ for P116(246–818); and $P116W_{681}$ to generate variant P116W681A. Detailed description on protein expression, purification and protein emptying has been reported previously[11].

Isotopic unesterified cholesterol transfer from lipoproteins

Human LDL (density 1.019–1.063 g/mL) and HDL (density 1.063–1.210 g/mL) were isolated through sequential gradient density ultracentrifugation, using potassium bromide for density adjustment, at 100,000 x *g* for 24 h with an analytical fixed-angle rotor (50.3, Beckman Coulter). The composition of both LDL and HDL, including total and unesterified cholesterol, triglycerides, and phospholipids, was determined enzymatically, using commercial kits adapted for a COBAS 6000/501c autoanalyzer (Roche Diagnostics), whereas apoB and apoA1 were determined by an immunoturbidimetric assay, using commercial kits adapted for a COBAS 6000/501c autoanalyzer. Radiolabeled LDLs and HDLs were prepared in the following way: 5 µCi of [1,2-^{3}H(N)] unesterified cholesterol (Perkin Elmer) was mixed with absolute ethanol, and the solvent was dried under a stream of N_2. LDL or HDL (0.5 mL, 2.5 g/L of ApoB or ApoA1) were added to the tubes containing the radiotracers, as appropriate, and then incubated for 16 h in a 37 °C bath[11]. The labeled LDLs and HDLs were re-isolated by gradient density ultracentrifugation and dialyzed against phosphate-buffered saline (PBS) through gel filtration chromatography. Specific activities of ^{3}H-cholesterol-containing LDLs and HDLs were 520 and 4,750 counts per minute (cpm)/nmol of unesterified cholesterol, respectively.

MPN M129 was grown to mid-log phase in 25 cm^2 cell culture flasks containing 5 mL SP4 medium and incubated at 37 °C with 5% CO_2. The medium was then replaced with 5 mL of SP4 lacking fetal bovine serum (FBS) and supplemented with [^{3}H] unesterified cholesterol–containing LDL or HDL (0.1 g/L apoB or apoA1, respectively). Cultures were incubated for 90 min, after which the medium was recovered, and surface-attached mycoplasmas were washed once with PBS, collected using a cell scraper, and resuspended in PBS. Radioactivity associated with both medium and cell fractions was measured by liquid scintillation counting, and cholesterol transfer per mL was determined, including control samples without cells.

The cholesterol transfer to P116 (the construct spanning residues 30 to 957, 1 g/L) was measured after adding either [^{3}H] unesterified cholesterol-containing LDLs or HDL (0.5 g/L of apoB or apoA1, respectively) and incubation at different times at 37 °C. Where indicated, mAb-3G9 and mAb-3B5 were added at a final concentration of 3 µg/mL. LDL, HDL, and P116 were separated by a HisTrap HP affinity. The radioactivity associated with each P116 and HDL fraction was measured through liquid scintillation counting. The percentage of [^{3}H] cholesterol transferred per mL was determined for each condition.

The specific activities for each radiotracer were used to calculate the amount of unesterified cholesterol from LDL or HDL to P116 or *MPN*. Human apoB and apoA1 levels were determined in both the LDL, HDL and purified P116 or *MPN* fractions by the immunoturbidimetric assays in the COBAS 6000/501c autoanalyzer.

Cholesterol efflux from cells to P116

Cellular cholesterol efflux to HDL and P116 (residues 30–957) was evaluated using a radiochemical method with H1299 human epithelial-like lung cells (ATCC® CRL-5803, Manassas, VA), CHO cells, CHO cells expressing SR-B1 (provided by Dr. Joerg Heere) and J774A1.1 mouse macrophages (ATCC® TIB67™). For this purpose, 3×10^5 cells/well were seeded in 6-well plates and grown for 72 h in complete Dulbecco's Modified Eagle's Medium (DMEM) high glucose with L-glutamine and sodium pyruvate (Corning, Glendale, AZ), supplemented with 10% FBS (Pan Biotech, Aidenbach, Germany) and 100 U/mL penicillin/streptomycin (Dominique Dutscher, Brumath, France). At that point, the cells were incubated with DMEM containing 1 µCi/well of [1α,2α(n)-3H] cholesterol (Perkin Elmer, Boston, MA) and 5% FBS for 48 h. Subsequently, the macrophages and lung cells were equilibrated overnight with 0.2% free fatty acid bovine serum albumin (Sigma Aldrich/Merck) in DMEM. This experiment was also conducted in macrophages, where efflux pathways were stimulated under controlled conditions. To activate the ABCA1/ABCG1-dependent cholesterol efflux, cells were treated during the equilibration period with 2 µM of the liver X receptor agonist T0901317 (Cayman Chemicals, Ann Arbor, MI)[36]. In separate experiments, 20 µM of the lipase inhibitor orlistat (Sigma-Aldrich/Merck) was applied to assess the potential contribution of lipase activity[37]. The following day, the media was removed, and the cells were incubated for 90 min with HDL, lipid-free apoA1 or P116 (100 µg/mL) in medium without any cholesterol supplement. For these in vitro analyses, human HDL and P116 were isolated as described above. The percentage of cholesterol efflux from cells to the acceptors was calculated by dividing the amount of radiolabeled cholesterol in the medium by the sum of radiolabeled cholesterol in both the medium and the cells, as determined by liquid scintillation counting at the end of the experiments.

Lipid extraction for mass spectrometry analyses

The lipid transfer to P116 (1 g/L) was measured after incubation with either LDL, HDL (0.5 g/L of apoB or apoA1, respectively), or H1299 human epithelial-like lung cells (1×10^6) at 37 °C for 90 min. The different P116 fractions were separated using a HisTrap HP affinity column. Metabolite extraction was performed by fractionating the protein samples into pools of species with similar physicochemical properties using appropriate combinations of organic solvents. Two extraction methods were employed based on the chemical class of the target analytes[38]. Platform 1 (Fatty Acyls, Bile Acids, Steroids, and Lysoglycerophospholipids Profiling): 125 µL of P116 (1 g/L) was mixed with 350 µL of methanol (spiked with metabolites not detected in unspiked human serum extracts) in 1.5 mL microtubes on ice. After brief vortexing, the samples were incubated for 1 h at −20 °C. The supernatants were collected following centrifugation at 18,000 × g for 15 min, dried, and reconstituted in 60 µL of methanol. The reconstituted samples were then centrifuged and transferred to vials for UHPLC-MS analysis. Platform 2 (Glycerolipids, Cholesteryl Esters, Sphingolipids, and Glycerophospholipids Profiling): 50 µL of P116 (1 g/L) was mixed with sodium chloride (50 mM) and chloroform/methanol (2:1) in 1.5 mL microtubes on ice. The extraction solvent was spiked with metabolites not detected in unspiked human serum extracts. After brief vortexing, the samples were incubated for 1 h at −20 °C. Following centrifugation at 16,000 × g for 15 min, the organic phase was

collected, and the solvent was removed. The dried extracts were reconstituted in 60 µL of acetonitrile/isopropanol (1:1), centrifuged (18,000 × g for 5 min), and transferred to vials for UHPLC-MS analysis. Randomized sample injections were performed for each analytical platform, with QC calibration and validation extracts uniformly interspersed throughout the batch run.

UHPLC-MS analyses

The lipidomic workflow consisted of the following steps: sample extraction → chromatographic separation → mass spectrometric detection → data processing → normalization and statistical analysis.

Lipidomic profiling was carried out using two ultra-high-performance liquid chromatography–mass spectrometry (UHPLC–MS) platforms, each optimized for specific lipid classes. Chromatographic separation was performed on ACQUITY UPLC systems (Waters Corp., Milford, USA). Mass spectrometric detection was carried out on a LCT Premier XE Time-of-Flight (ToF) (Waters Corp.) for Lipidomics Platform 1 and on a Xevo G2 QTof (Waters Corp.) for Lipidomics Platform 2. The full chromatographic and MS conditions are summarized in Supplementary Table 2.

To ensure analytical robustness, pooled quality control (QC) extracts were injected regularly throughout the batch sequence. Retention time stability was generally <6 s (injection-to-injection), and mass accuracy was maintained at <5 ppm for ions in the m/z 400–1000 range and <1.2 mDa for ions in the m/z 50–400 range.

Data were processed using the TargetLynx application manager for MassLynx 4.1 software (Waters Corp., Milford, USA). Predefined retention time and mass-to-charge ratio (Rt–m/z) pairs corresponding to known metabolites were entered into the software, which extracted ion chromatograms (mass tolerance window = 0.05 Da). These chromatograms were peak-detected and noise-reduced in both the LC and MS domains, ensuring that only true metabolite-related signals were included.

Chromatographic peak areas were generated for each metabolite in each sample. For normalization, representative internal standards were included for every major lipid class analyzed. MS detection response curves were constructed using these standards to define linear detection ranges. Assuming similar ionization and detector responses within a lipid class, all metabolites were normalized against their respective class-specific internal standards. Final normalized peak areas were expressed relative to the sum of all detected features per sample to account for potential variability in sample preparation and instrument response. Normalized data were then classified according to their chemical properties following the comprehensive system proposed by Fahy et al.[39] under the International Lipid Classification and Nomenclature Committee and expressed in the LIPID MAPS initiative (http://www.lipidmaps.org).

Immunoassays

Twenty-five patients with an infection by *MPN* based on a positive result with the Liaison *MPN* IgG, IgM kit (DiaSorin, Italy) were selected. Similarly, six sera from healthy donors and testing negative for the Liaison *MPN* IgG, IgM kit were also selected. No sex, gender, race, ethnicity, or other socially relevant group information was collected; only clinical diagnosis and IgG/IgM anti-*MPN* values were recorded. In both cases, we used a 1/100 dilution of the patient sera. Indirect ELISA assays were performed on 96 well plates Immulon 4 HBX 96 well plates (ThermoFisher) incubating 1 µg of each antigen at 4 °C overnight. 1/100 dilutions of each patient sera were added to the plate and detected using and anti-human IgG antibody conjugated with HRP (Thermofisher Scientific). Upon incubation for 30 min with 100 µl of substrate (Thermofisher Scientific), 100 µl of sulphuric acid 25% were added to stop the reaction, and absorbance was read at 450 nm on a Triturus ELISA instrument (Grifols) device. Reference filter was set at 620 nm.

Bacterial strains and culture conditions

The *MPN* M129 and *MPN*-Venus strains[18] were grown in cell culture flasks containing SP4 medium and incubated at 37 °C with 5% CO_2. Surface-attached mycoplasmas were collected using a cell scraper and resuspended in SP4 medium.

Polyclonal and monoclonal antibody generation and purification

Two BALB/C mice were serially immunized with four intraperitoneal injections, each one containing 150 µg of recombinant P116 ectodomain (residues 30–957) in 200 µL of PBS with no adjuvants[11]. The last injection was delivered four days before splenectomy. Isolated B lymphocytes from the immunized mice were fused to NSI myeloma cells[40] to obtain stable hybridoma cell lines producing mAb, as previously described[41]. Supernatants from hybridoma cell lines derived from single fused cells were first investigated by indirect ELISA screening against the recombinant P116 ectodomain. Positive clones were also tested by Western blot against protein profiles from *MPN* cell lysates and by immunofluorescence using whole, non-permeabilized *MPN* cells. Only those clones with supernatants revealing a single 116 kDa band in protein profiles and also exhibiting a consistent fluorescent staining of *MPN* cells were selected and used in this work. Polyclonal sera were obtained by cardiac puncture of properly euthanized mice just before splenectomy and tittered using serial dilutions of the antigen. The titer of each polyclonal serum was determined as the IC_{50} value from four-parameter logistic plots and found to be approximately 1/4000 for both sera. The monoclonal antibody P116 mAb-3B5 was selected by ELISA screening using P116 30-957 construct, but tested negative against the P116 central region construct (residues 246–818). The mAb-3G9 was selected by ELISA screening and showed high specificity to P116 in Western blotting analysis and immunofluorescence microscopy of living *MPN* cells[11]. To ensure the produced antibody was monospecific, hybridoma cells producing mAb–3G9 were cloned by limiting dilution and subjected to a second cloning step using the BD FACS Discover S8, selecting cells by size and complexity, and sorting in single cell mode.

As indicated in the different experiments, mAb-3G9 was used unpurified from supernatants of exponentially grow hybridoma cell cultures in Roswell Park Memorial Institute medium (RPMI) 1640 supplemented with 8% fetal bovine serum. For cryoelectron microscopy studies, mAb-3G9 was purified from 100 mL aliquots of cell culture supernatants. Briefly, supernatants were diluted twice in 20 mM sodium phosphate buffer pH 7.0 and submitted to 1 mL HiTrap Protein G columns (cytiva) previously equilibrated in this buffer. After washing the column with 10 volumes of phosphate buffer, mAb was eluted in 0.1 M glycine pH 2.7 on tubes with a 1/10 volume of Tris 1 M pH 9. Pooled eluted fractions were concentrated using a 50 K Amicon Ultra 15 centrifugal filters to a 1 mL final volume and washed three times with PBS. The concentrated antibody sample was further purified using a Superose 6 Increase 10/300 GL column previously equilibrated in PBS, and the eluted fractions in the range of 150 kDa were finally concentrated to a 0.5 mL volume also using a 50 K Amicon.

Monoclonal antibody sequencing

Cloned hybridoma cells producing mAb-3G9 were cultured in T75 flasks using RPMI 1640 medium supplemented with 8% fetal bovine serum and grown until 50% confluence. RNA extraction was performed using the RNeaSY Mini Kit (QIAGEN) and 5×10^6 hybridoma cells by direct lysis of the cell pellet and omitting the optional DNase digestion step. Then, the cDNAs coding for the heavy and light chains were amplified by SMART RT-PCR following the simplified workflow described by Meyer et al.[42] with few modifications. Briefly, the first strand was obtained by incubating 500 ng of total RNA, 1 µL of primers mIGK RT, mIGL RT or mIGHG RT at 10 µM in separate tubes, 1 µL of

10 mM dNTPs and 11 μL of RNase-free water at 65 °C for 5 min. Then, 4 μL of the first strand buffer of M-MLV reverse transcriptase (Invitrogen), 2 μL 100 mM DTT, 1 μL RNaseOut and 1 μL Template-Switch primer 100 μM were added to each tube. After incubating 2 min at 37 °C 1 μL of M-MLV reverse transcriptase (Invitrogen) was added to each tube, which were incubated for 50 min at 37 °C and 15 min at 70 °C. The touch down PCR reaction was performed as originally described using the Phusion thermopolymerase (Thermo Scientific) using 3 μL of each cDNA obtained in the previous step. The resulting PCR products were subjected to a 1% agarose gel and bands corresponding to the cDNAs of the heavy and kappa light chains (Supplementary Fig. 9a). Next, 700 bp and 600 bp bands corresponding to the RT-PCR products of the heavy and kappa light chains, respectively were excised from the gel, and the purified DNAs were ligated to the pBSKII vector previously digested with EcoRV. Ligation reactions were then transformed to competent *Escherichia coli* XL1-blue cells and several colonies were selected and cultured to obtain the plasmid DNAs. A total of 9 plasmids bearing cDNAs from the heavy chain and 8 plasmids containing cDNAs from the kappa chain were submitted to Sanger sequencing on an ABI 3730 DNA Analyzer using the BigDye Terminator method and the reverse universal primer. The obtained DNA sequences were trimmed to remove the plasmid sequences using the VectorStrip application from the mEMBoss suite, translated to the six possible read frames and aligned using the ClustaX v2.1 application (http://www.clustal.org/clustal2). Eight out of nine sequences for the kappa chain and five out eight sequences from the kappa light chain contained sequences to the corresponding immunoglobulin chains. Aligned amino acid sequences coding for heavy chains were 95% identical starting from the first Met residue, and sequences coding for kappa light chains were 100% identical starting from the first Met residue (Supplementary Fig. 9b). The consensus sequence from each alignment was chosen as the complementary determining sequence in each of the chains of the P116 mAb-3G9 antibody.

Single-particle cryoEM P116-mAb complex

For single-particle cryo-electron microscopy (cryoEM), a 3 μL drop of purified P116-mAb complex (0.2 mg/mL in 20 mM Tris pH 7.4 and 150 mM NaCl buffer) was applied to glow-discharged C-Flat™ holey grids (CF-1.2/1.3; 300 mesh), 5 s blotting (−3 blotting force) and vitrified in liquid ethane using a Vitrobot Mark IV (Thermo Fisher Scientific) set to 4 °C and 95 % humidity. Cryo-EM grids were stored at liquid nitrogen temperature.

Movies of P116-mAb complex were collected on a Glacios electron microscope operated at 200 kV (IBMB-CSIC CryoEM Platform). Imaging was performed using EPU at a nominal magnification of ×150,000 (0.96 Å/pixel) at 200 kV Glacios (Thermo Fisher Scientific) electron microscope equipped with Falcon 4 detector (Thermo fisher Scientific). A total of 5859 movies were collected. The camera was operated in counting mode with a dose rate of 7.24 electrons per $Å^2\ s^{-1}$, resulting in a total dose of 39.70 electrons per $Å^2$. Defocus values ranged from −1.0 to −2.5 μm.

CryoSPARC v4[43] was used to process the cryoEM data. Particles were selected with the Blob picker using a particle diameter of 150–300 Å. Particles were extracted and classified in 2D. For the final processing, the 2D particles containing the complex were selected, remaining a total of 412,947 particles which were used to generate an ab initio reconstruction with three classes followed by a subsequent non-uniform heterogeneous refinement with the largest class. Finally, a model with a resolution of 5.06 Å was obtained (Supplementary Table 3).

Docking, tracing and refinement of all the structures was performed alternating interactive and automatic cycles with programs Coot and Phenix. The final refined structure has been deposited in the PDB with code: 9GVG and the map in the EMDB with code: 51635.

Effect of mAb on mycoplasma cell growth

Growth rates of *MPN* cultures were determined using an adaptation of the colorimetric protocol described by Karr and colleagues[44]. *MPN* M129 strain was grown to mid-log phase in 25 cm^2 flasks with 5 mL SP4 medium. Attached cells were scraped off, recovered by centrifugation at 15,000 x *g* and resuspended in 3 mL of fresh SP4 medium, SP4 medium supplemented with a 1/200 dilution of P116 mAb-3G9 or mAb-3B5 hybridoma cell culture supernatant in PBS, or SP4 medium supplemented with RPMI 1640 medium also diluted 1/200 in PBS as control. Then, 300 μL of the cellular suspension were seeded in four different wells of a 96-well plate and serially diluted 1/3 until reaching a 1/243 using the same respective media described above. The resulting 96-well plated was sealed with transparent tape, placed into a Tecan Sunrise Absorbance Microplate Reader (Tecan), and incubated at 37 °C for 8 days. During the incubation time, absorbance at 550 nm for each well was recorded each 15 min to quantify the medium acidification resulting from the mycoplasma growth, which turns the color of the phenol red indicator from red to yellow. Curves of absorbance vs time were plotted for each well and the inflection point of each curve was determined by iteration using the Excel application controlled by a Phyton script. Next, the inflection points were plotted, using the Napierian logarithm of the dilution as the x coordinate for each dilution. Once all the inflection points were plotted, the slope (μ, growth rate constant) was inferred by linear regression, and the doubling time (g) was obtained according to the general equation for exponential growth of bacteria ($g = \ln 2/(1/\mu)$).

Interaction of MPN with human atherosclerotic plaques ex vivo

Carotid endarterectomy specimens were obtained within one hour of surgical resection. Immediately after collection, the specimens were placed in phosphate-buffered saline for processing. The specimens were then evaluated under a dissecting microscope and cut into small pieces. Fragments containing atherosclerotic plaque and fragments from the distal boundary of the plaque were collected for further analysis.

The *MPN* strain M129 expressing the fluorescent protein Venus[18] was grown in cell culture flasks containing SP4 medium and incubated at 37 °C and 5% CO_2. Surface-attached mycoplasmas were collected using a cell scraper and resuspended in SP4 medium. Co-cultures were performed in IBIDI eight-well chamber slides, being each well seeded with 1×10^5 mycoplasma cfus in 200 μL of 0.22 μm filtered SP4 medium and a small piece of healthy carotid tissue (HT) or atherosclerotic plaque tissue (AP). In some experiments, mAb-3G9 and mAb−3B5 were added at a final concentration of 3 μg/mL at the time of inoculation. Phase contrast (PhC) and epifluorescence microscopy images of MPN cells incubated with human carotid tissue fragments were acquired using an inverted Nikon Eclipse TE2000-E microscope. HT and AP were analyzed in parallel. After inoculation with *MPN* Venus strain cells, images were acquired at 0 h, 24 h, and 48 h, focusing on the same tissue regions across time points. YFP fluorescence (excitation 490/510 nm, emission 520/550 nm) was detected with an Orca Fusion camera (Hamamatsu) controlled by NIS-Elements BR software (Nikon).

Quantification of MPN localization and proliferation was performed by measuring the percentage increase in fluorescent area from 0 h to 48 h using four independent biological replicates.

Biodistribution of MPN into atherosclerotic mice

Female wild-type mice and $LDLR^{-/-}$ mice on the C57BL/6 background were purchased from Jackson Laboratories (Bar Harbor, ME; #000664 and #002207, respectively), and housed under pathogen-free conditions at the Clinica Universidad de Navarra animal facility. Mice were kept in a temperature-controlled (22 °C) room with a 12-hour light/dark cycle, and food and water were provided ad libitum. We used 4–5^{th}-month-old mice fed with a Western-type diet (TD.88137, Harlan

Teklad, Madison, WI, containing 21% fat and 0.2% cholesterol) for 8 weeks.

To investigate the in vivo biodistribution of Mycoplasma using single SPECT/CT, the non-pathogenic *MPN* strain CV8[45] was cultured in Hayflick for 3–4 days in T75 flask. Cells were washed twice and scraped in 1 ml of PBS. A bacterial suspension containing 10^7 CFUs was radiolabeled by incubating it with 5,96 MBq of [^{111}In]In-oxine at 37 °C for 15 min. Following radiolabeling, 100 µL (3.34 ± 0.03 MBq) of the radiolabeled Mycoplasma was injected in the vein tail. Six hours post-injection, images were acquired using a SPECT/CT scanner (U-SPECT6/E-class, (MILabs, Utrecht, The Netherlands). During image acquisition, the animals were placed in the prone position on the scanner bed under continuous anesthesia with isoflurane (2% in 100% O_2), and a 60-minute whole body scan was performed. After SPECT acquisition, CT scans were conducted to obtain anatomical reference, using a tube setting of 55 kV and 0.33 mA. SPECT and CT images were reconstructed using the ^{111}In photopeaks at 170 and 245 keV with a 20% energy window. A calibration factor was applied to determine activity (MBq/mL), and attenuation correction was performed using the CT attenuation map. The animals were subsequently sacrificed, exsanguinated, and perfused with saline, after which the heart and major vessels were excised for SPECT/CT imaging. Liver-associated activity was quantified by measuring Bq of [^{111}In]In-oxine with a gamma counter.

Experiments were conducted in a blind manner concerning the origin of the specimens to reduce bias. Plasma total cholesterol and triglycerides were determined enzymatically using commercial kits adapted for a COBAS 6000/501c autoanalyzer (Roche Diagnostics, Rotkreuz, Switzerland). Liver lipids were extracted using isopropyl alcohol-hexane (2:3, v/v), and the lipid layer was collected, evaporated, and resuspended in 0.5% (w/v) sodium cholate (Serva, Heidelberg, Germany). Cholesterol and triglycerides were determined using commercial kits adapted for the COBAS 6000/501c autoanalyzer.

Liver samples stored at −80 °C were homogenized with an Ultra-Turrax (IKA), and total DNA was extracted using the DNeasy® UltraClean® Microbial Kit (Qiagen) according to the manufacturer's instructions. For standard curve generation, the *MPN* CV8 strain was cultured for 72 h. Cells were harvested, and one aliquot was plated on Hayflick agar to estimate CFU/mL. The remaining culture was centrifuged (15,000 x g, 5 min), and the pellet was processed for DNA extraction. DNA concentration was measured using a NanoDrop One spectrophotometer (Thermo Scientific), and integrity was assessed by 1% agarose gel electrophoresis. Quantitative PCR (qPCR) was performed with SYBR Premix Ex Taq II (Tli RNaseH Plus; Takara) on an AriaMx Real-Time PCR System (Agilent Technologies). The following primers targeting the *adk* gene (mpn185) were used: forward 5′-CCGTTTGGTTTGTCCTAGTTGTGGTAGTG-3′ and reverse 5′-GATTACCGCTTCCGTGTCATCATTGC-3′. Murine hearts were fixed in 4% paraformaldehyde for 4 h at 4 °C, washed in PBS for 1 h, and incubated overnight in 30% sucrose. Tissues were embedded in OCT and immediately frozen. Hearts were sectioned transversely at 6 µm using a Leica CM1950 cryostat (Leica Biosystems, Wetzlar, Germany). To quantify aortic lesion size, serial sections were stained with Oil Red O (Sigma-Aldrich). Plaque areas were outlined, and the mean lesion size was calculated across at least five sections per mouse[46].

Statistical methods

Data are presented as the mean ± standard deviation (SD). Unpaired t-tests were used to compare the differences between two groups. Differences between two groups were analyzed using unpaired t-tests, while comparisons across more than two groups were performed using one-way ANOVA followed by Tukey's multiple comparisons post-test. Associations between variables were assessed using Pearson's correlation coefficient. A chi-square test was used to compare the distribution of human antibody reactivity against different P116 constructs. GraphPad Prism version 8.0.2 for Windows (GraphPad Software, San Diego, CA) was used to perform all statistical analyses. A *P*-value ≤ 0.05 was considered statistically significant.

Reporting summary

Further information on research design is available in the Nature Portfolio Reporting Summary linked to this article.

Data availability

Data for the relative intensity of identified lipid compounds generated in this study have been deposited in CORA. Repositori de Dades de Recerca (https://dataverse.csuc.cat/previewurl.xhtml?token=c28f573c-18ee-45f6-a3d8-323087d1342d). The analytical methods, and study materials will be available to other researchers for purposes of reproducing the results or replicating the procedure upon reasonable request. Source data are provided with this paper.

References

1. Tsiodras, S., Kelesidis, I., Kelesidis, T., Stamboulis, E. & Giamarellou, H. Central nervous system manifestations of Mycoplasma pneumoniae infections. *J. Infect.* **51**, 343–354 (2005).
2. Ferwerda, A., Moll, H. A. & de Groot, R. Respiratory tract infections by Mycoplasma pneumoniae in children: a review of diagnostic and therapeutic measures. *Eur. J. Pediatr.* **160**, 483–491 (2001).
3. Atkinson, T. P., Balish, M. F. & Waites, K. B. Epidemiology, clinical manifestations, pathogenesis and laboratory detection of Mycoplasma pneumoniae infections. *FEMS Microbiol Rev.* **32**, 956–973 (2008).
4. Parrott, G. L., Kinjo, T. & Fujita, J. A Compendium for Mycoplasma pneumoniae. *Front Microbiol* **7**, 513 (2016).
5. Meyer Sauteur, P. M. et al. Mycoplasma pneumoniae: delayed re-emergence after COVID-19 pandemic restrictions. *Lancet Microbe* **5**, e100–e101 (2024).
6. Nordholm, A. C. et al. Mycoplasma pneumoniae epidemic in Denmark, October to December, 2023. *Eur. Surveill.* **29**, 2300707 (2024).
7. Himmelreich, R., Plagens, H., Hilbert, H., Reiner, B. & Herrmann, R. Comparative analysis of the genomes of the bacteria Mycoplasma pneumoniae and Mycoplasma genitalium. *Nucleic Acids Res.* **25**, 701–712 (1997).
8. Gaspari, E. et al. Model-driven design allows growth of Mycoplasma pneumoniae on serum-free media. *NPJ Syst. Biol. Appl* **6**, 33 (2020).
9. Broto, A. et al. Engineering Mycoplasma pneumoniae to bypass the association with Guillain-Barre syndrome. *Microbes Infect.* **26**, 105342 (2024).
10. Dahl, J. The role of cholesterol in mycoplasma membranes. *Subcell. Biochem.* **20**, 167–188 (1993).
11. Sprankel, L. et al. Essential protein P116 extracts cholesterol and other indispensable lipids for Mycoplasmas. *Nat. Struct. Mol. Biol.* **30**, 321–329 (2023).
12. Higuchi, M. L. et al. Detection of Mycoplasma pneumoniae and Chlamydia pneumoniae in ruptured atherosclerotic plaques. *Braz. J. Med Biol. Res.* **33**, 1023–1026 (2000).
13. Higuchi Mde, L. et al. Coinfection with Mycoplasma pneumoniae and Chlamydia pneumoniae in ruptured plaques associated with acute myocardial infarction. *Arq. Bras. Cardiol.* **81**, 12–22 (2003).
14. Ramires, J. A. & Higuchi Mde, L. [Mycoplasma pneumoniae and Chlamydia pneumoniae are associated to inflammation and rupture of the atherosclerotic coronary plaques]. *Rev. Esp. Cardiol.* **55**, 2–9 (2002).

15. Damy, S. B. et al. Mycoplasma pneumoniae and/or Chlamydophila pneumoniae inoculation causing different aggravations in cholesterol-induced atherosclerosis in apoE KO male mice. *BMC Microbiol.* **9**, 194 (2009).
16. Feingold, K. R. Introduction to Lipids and Lipoproteins. in *Endotext* (eds. Feingold, K. R., et al.) (South Dartmouth (MA), 2000).
17. Linton, M. F. et al. The Role of Lipids and Lipoproteins in Atherosclerosis. in *Endotext* (eds. Feingold, K. R., et al.) (South Dartmouth (MA), 2000).
18. Mariscal, A. M. et al. Tuning Gene Activity by Inducible and Targeted Regulation of Gene Expression in Minimal Bacterial Cells. *ACS Synth. Biol.* **7**, 1538–1552 (2018).
19. Razin, S., Yogev, D. & Naot, Y. Molecular biology and pathogenicity of mycoplasmas. *Microbiol Mol. Biol. Rev.* **62**, 1094–1156 (1998).
20. Svenstrup, H. F., Nielsen, P. K., Drasbek, M., Birkelund, S. & Christiansen, G. Adhesion and inhibition assay of Mycoplasma genitalium and M. pneumoniae by immunofluorescence microscopy. *J. Med Microbiol.* **51**, 361–373 (2002).
21. Vizarraga, D. et al. Immunodominant proteins P1 and P40/P90 from human pathogen Mycoplasma pneumoniae. *Nat. Commun.* **11**, 5188 (2020).
22. Phillips, M. C. Molecular mechanisms of cellular cholesterol efflux. *J. Biol. Chem.* **289**, 24020–24029 (2014).
23. Qiu, X. et al. Crystal structure of cholesteryl ester transfer protein reveals a long tunnel and four bound lipid molecules. *Nat. Struct. Mol. Biol.* **14**, 106–113 (2007).
24. Razin, S. & Tully, J. G. Cholesterol requirement of mycoplasmas. *J. Bacteriol.* **102**, 306–310 (1970).
25. Rottem, S. Membrane lipids of mycoplasmas. *Biochim Biophys. Acta* **604**, 65–90 (1980).
26. Rottem, S., Adar, L., Gross, Z., Ne'eman, Z. & Davis, P. J. Incorporation and modification of exogenous phosphatidylcholines by mycoplasmas. *J. Bacteriol.* **167**, 299–304 (1986).
27. Yus, E. et al. Impact of genome reduction on bacterial metabolism and its regulation. *Science* **326**, 1263–1268 (2009).
28. Kornspan, J. D. & Rottem, S. The phospholipid profile of mycoplasmas. *J. Lipids* **2012**, 640762 (2012).
29. Safronova, N., Junghans, L. & Saenz, J. P. Temperature change elicits lipidome adaptation in the simple organisms Mycoplasma mycoides and JCVI-syn3B. *Cell Rep.* **43**, 114435 (2024).
30. Momiyama, Y., Ohmori, R., Taniguchi, H., Nakamura, H. & Ohsuzu, F. Association of Mycoplasma pneumoniae infection with coronary artery disease and its interaction with chlamydial infection. *Atherosclerosis* **176**, 139–144 (2004).
31. Chung, W. S., Hsu, W. H., Lin, C. L. & Kao, C. H. Mycoplasma pneumonia increases the risk of acute coronary syndrome: a nationwide population-based cohort study. *QJM* **108**, 697–703 (2015).
32. Trefts, E., Gannon, M. & Wasserman, D. H. The liver. *Curr. Biol.* **27**, R1147–R1151 (2017).
33. Poddighe, D. Mycoplasma pneumoniae-related hepatitis in children. *Micro. Pathog.* **139**, 103863 (2020).
34. Hu, J. et al. Insight into the Pathogenic Mechanism of Mycoplasma pneumoniae. *Curr. Microbiol.* **80**, 14 (2022).
35. Mazzolini, R. et al. Engineered live bacteria suppress Pseudomonas aeruginosa infection in mouse lung and dissolve endotracheal-tube biofilms. *Nat. Biotechnol.* **41**, 1089–1098 (2023).
36. Cedo, L. et al. LDL Receptor Regulates the Reverse Transport of Macrophage-Derived Unesterified Cholesterol via Concerted Action of the HDL-LDL Axis: Insight From Mouse Models. *Circ. Res.* **127**, 778–792 (2020).
37. Saraswathi, V. & Hasty, A. H. The role of lipolysis in mediating the proinflammatory effects of very low density lipoproteins in mouse peritoneal macrophages. *J. Lipid Res* **47**, 1406–1415 (2006).
38. Barr, J. et al. Liquid chromatography-mass spectrometry-based parallel metabolic profiling of human and mouse model serum reveals putative biomarkers associated with the progression of nonalcoholic fatty liver disease. *J. Proteome Res* **9**, 4501–4512 (2010).
39. Fahy, E. et al. A comprehensive classification system for lipids. *J. Lipid Res* **46**, 839–861 (2005).
40. Kohler, G. & Milstein, C. Continuous cultures of fused cells secreting antibody of predefined specificity. *Nature* **256**, 495–497 (1975).
41. Guasch, A. et al. Structure of P46, an immunodominant surface protein from Mycoplasma hyopneumoniae: interaction with a monoclonal antibody. *Acta Crystallogr D. Struct. Biol.* **76**, 418–427 (2020).
42. Meyer, L. et al. A simplified workflow for monoclonal antibody sequencing. *PLoS One* **14**, e0218717 (2019).
43. Punjani, A., Rubinstein, J. L., Fleet, D. J. & Brubaker, M. A. cryoSPARC: algorithms for rapid unsupervised cryo-EM structure determination. *Nat. Methods* **14**, 290–296 (2017).
44. Karr, J. R. et al. A whole-cell computational model predicts phenotype from genotype. *Cell* **150**, 389–401 (2012).
45. Montero-Blay, A. et al. Bacterial expression of a designed single-chain IL-10 prevents severe lung inflammation. *Mol. Syst. Biol.* **19**, e11037 (2023).
46. Rotllan, N. et al. Antagonism of miR-148a attenuates atherosclerosis progression in APOB(TG)Apobec(−/−)Ldlr(+/-) mice: A brief report. *Biomed. Pharmacother.* **153**, 113419 (2022).

Acknowledgements

This work was partly funded by the Instituto de Salud Carlos III and FEDER "Una manera de hacer Europa" grant PI2300232 (to J.E.-G.). N.R. was funded by Agencia Estatal de Investigación (AEI/10.13039/501100011033 and CNS2023-144119) within the Subprograma Ramón y Cajal (RYC-201722879) and by MICINN-Spain grant PID2022-137186OB-I00. CIBERDEM is an Instituto de Salud Carlos III project. I.F. and J.P. were funded by MICINN-Spain grant PID2021-125632OB-C21 and PID2021-125632OB-C22. The authors acknowledge funding from Project, IU16-014045 (CRYO-TEM) from Generalitat de Catalunya, and by "ERDF A way of making Europe", by the European Union.

Author contributions

D.V.: Conceptualization, Methodology, Validation, Formal analysis, Writing – review & editing. M.M.: Conceptualization, Methodology, Validation, Formal analysis, Writing – review & editing. N.R.: Conceptualization, Methodology, Validation, Formal analysis, Funding, Writing – review & editing. The first authors (D.V., M.M., and N.R.) contributed equally to this work. The order of their names was assigned randomly, and each author may be cited as a first author. J.M.: Methodology, Validation, Formal analysis. D.S.: Methodology. M.Ca.: Methodology, Writing – review & editing. B.S.: Methodology. L.V-R.: Methodology, Writing – review & editing. P.G.: Methodology, Validation, Formal analysis. F.P.: Methodology, Validation, Formal analysis. M.Co.: Methodology, Validation, Formal analysis, Writing – review & editing. W.W.: Methodology, Validation, Formal analysis. I.R-A.: Methodology, Writing – review & editing, L.S.: Funding, Writing – review & editing. J.P.: Conceptualization, Methodology, Validation, Formal analysis, Funding, Writing – original draft, Writing – review & editing. I-F.: Conceptualization, Methodology, Validation, Formal analysis, Funding, Writing – original draft, Writing – review & editing. J.C.E-G.: Conceptualization, Methodology, Validation, Formal analysis, Funding, Writing – original draft, Writing – review & editing. These authors jointly supervised this work: J.P., I.F., J.C.E.-G.

Competing interests

The authors declare no competing interests.

Additional information

Supplementary information The online version contains supplementary material available at https://doi.org/10.1038/s41467-025-66129-5.

Correspondence and requests for materials should be addressed to Jaume Piñol, Ignacio Fita or Joan Carles Escolà-Gil.

Peer review information *Nature Communications* thanks Sander Kooijman, who co-reviewed with Mohan Li, Jeremy Derrick, and the other, anonymous, reviewer(s) for their contribution to the peer review of this work. A peer review file is available.